CrossMark

Magnetic Reconnection in Black Hole Magnetospheres: Lepton Loading into Jets, Superluminal Radio Blobs, and Multiwavelength Flares

Shigeo S. Kimura[1,2] ⓘ, Kenji Toma[1,2] ⓘ, Hirofumi Noda[3] ⓘ, and Kazuhiro Hada[4,5] ⓘ
[1] Frontier Research Institute for Interdisciplinary Sciences, Tohoku University, Sendai 980-8578, Japan; shigeo@astr.tohoku.ac.jp
[2] Astronomical Institute, Graduate School of Science, Tohoku University, Sendai 980-8578, Japan
[3] Department of Earth and Space Science, Graduate School of Science, Osaka University, 1-1 Machikaneyama, Toyonaka, Osaka 560-0043, Japan
[4] Mizusawa VLBI Observatory, National Astronomical Observatory of Japan, 2-12 Hoshigaoka, Mizusawa, Oshu, Iwate 023-0861, Japan
[5] Department of Astronomical Science, The Graduate University for Advanced Studies (SOKENDAI), 2-21-1 Osawa, Mitaka, Tokyo 181-8588, Japan

Abstract

Supermassive black holes in active galactic nuclei launch relativistic jets, as indicated by observed superluminal radio blobs. The energy source of these jets is widely discussed in the theoretical framework of the Blandford–Znajek process, the electromagnetic energy extraction from rotating black holes (BHs), while the formation mechanism of the radio blobs in the electromagnetically dominated jets has been a long-standing problem. Recent high-resolution magnetohydrodynamic simulations of magnetically arrested disks exhibited magnetic reconnection in a transient magnetically dominated part of the equatorial disk near the BH horizon, which led to a promising scenario of efficient MeV gamma-ray production and subsequent electron–positron pair loading into the BH magnetosphere. We develop this scenario to build a theoretical framework on energetics, timescales, and particle number density of the superluminal radio blobs and discuss observable signatures in other wave bands. We analytically show that the nonthermal electrons emit broadband photons from optical to multi-MeV bands. The electron–positron pairs produced in the magnetosphere are optically thick for synchrotron self-absorption, so that the injected energy is stored in the plasma. The stored energy is enough to power the superluminal radio blobs observed in M87. This scenario predicts rather dim radio blobs around Sgr A*, which are consistent with no clear detection by current facilities. In addition, this scenario inevitably produces strong X-ray flares in a short timescale, which will be detectable by future X-ray satellites.

1. Introduction

Relativistic jets are ubiquitously launched by black holes (BH), such as stellar mass BHs in X-ray binaries, central engines of gamma-ray bursts (GRBs), and supermassive BHs (SMBHs) in active galactic nuclei (AGNs). However, the production mechanisms of jets are still unclear. In the context of GRBs, the energy injection by neutrino annihilation is actively discussed (Kumar & Zhang 2015; Kimura 2022), whereas this mechanism does not work in X-ray binaries or AGNs. In these systems, the energy sources of jets are likely the spin energy of BHs threaded by magnetic fields, which can be extracted via the Blandford–Znajek (BZ) process (Blandford & Znajek 1977; Komissarov 2004; Toma & Takahara 2016; Kimura et al. 2021a).

General relativistic magnetohydrodynamic (GRMHD) simulations of magnetized accretion disks show that the dilute polar region can form magnetosphere with $\sigma_B = B^2/(4\pi n_e m_e c^2) \gg 1$ around a BH, where the BZ process works (McKinney & Gammie 2004; Tchekhovskoy et al. 2011; Narayan et al. 2012; Takahashi et al. 2016; Nakamura et al. 2018; Event Horizon Telescope Collaboration et al. 2019a; Mizuno 2022). GRMHD simulations indicate that accretion flows can be classified into two modes (Narayan et al. 2012): one is the standard and normal evolution (SANE) in which the magnetic fields are

weak and turbulent, while the other is the magnetically arrested disk (MAD) in which magnetic fields are strong and mostly ordered. The electromagnetic power of jets in the MAD mode is higher than that for the SANE mode (Tchekhovskoy et al. 2011; Event Horizon Telescope Collaboration et al. 2019a; Cruz-Osorio et al. 2022), and thus, many believe that MADs are responsible for production of relativistic jets. This picture is observationally supported by the estimate of magnetic flux using core-shift measurements of radio galaxies (Zamaninasab et al. 2014) and the polarization map of M87 (Event Horizon Telescope Collaboration et al. 2021a, 2021b).

However, it has been a long-standing problem how BH magnetospheres produce superluminal radio blobs, which are observed as a remarkable indication of relativistic jets (Cohen et al. 1971; Whitney et al. 1971; Begelman et al. 1984; Blandford et al. 2019; Hada 2019). The previous GRMHD simulations and studies of nonthermal processes around BHs implied that the magnetosphere becomes too dilute to emit radiation ascribed to the superluminal radio blobs (Levinson & Rieger 2011; Mościbrodzka et al. 2011; Toma & Takahara 2012; Kimura et al. 2014; Kimura & Toma 2020; Kawashima et al. 2021).[6] General relativistic (GR) particle-in-cell (PIC) simulations have not provided any hints of sufficient e^+e^- pair production, either (Levinson & Cerutti 2018; Chen et al. 2018; Parfrey et al. 2019; Kisaka et al. 2020).

---

[6] Note that the wind or coronal regions of MADs outside the magnetosphere ($\sigma_B \lesssim 1$) does not have free energy sufficient for acceleration to relativistic speed (e.g., Sądowski et al. 2013; Cemeljic et al. 2022).
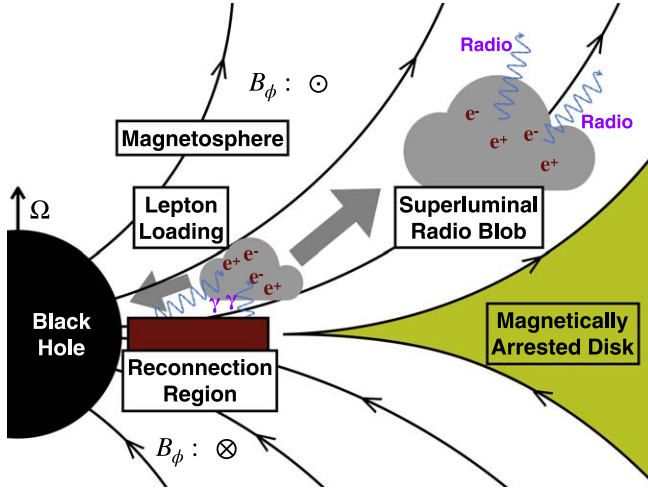
Figure 1. Schematic picture of our lepton loading scenario. The magnetic field above and below the midplane of a MAD transiently pushes out the accreting matter in a nonaxisymmetric manner, which triggers magnetic reconnection with $\sigma_B \gg 1$. The magnetic reconnection accelerates nonthermal electrons that emit luminous gamma rays. A fraction of these gamma rays interact with each other, producing e^+e^- pairs above and below the reconnection region. The pair plasma is thermalized, and subsequently will be accelerated to relativistic speed. We can observe it as a superluminal radio blob after it becomes optically thin.

Recently, Ripperda et al. (2022) proposed a promising scenario of particle loading into jets. In the MAD state, the strong and ordered magnetic fields can temporally halt the accretion process. Then, the accreting matter is accumulated outside a certain radius. This situation leads to development of magnetic Rayleigh–Taylor instability, which enables the matter to accrete to the BH with a spiral structure (McKinney et al. 2012; White et al. 2019). Based on recent extremely high-resolution GRMHD simulations, the magnetic fields above and below the equatorial plane push out the accreting matter in the low-density spiral, which triggers magnetic reconnection with $\sigma_B \gg 1$ at the equatorial plane in the BH magnetosphere (Ripperda et al. 2022). Such a relativistic magnetic reconnection accelerates nonthermal particles very efficiently (Zenitani & Hoshino 2001, 2007; Sironi & Spitkovsky 2014; Guo et al. 2014, 2020). The nonthermal electrons emit MeV gamma rays via synchrotron radiation, which interact with each other and produce e^+e^- pairs. Ripperda et al. (2022) pointed out that this mechanism can achieve the pair multiplicity of 10^8 and they emit radio to optical photons by back-of-the-envelope estimates.

In this Letter, we further examine this lepton loading scenario and discuss observable signatures from the magnetic reconnection events. We analytically compute the synchrotron spectrum and pair production rate, and confirm that this process can load a large amount of e^+e^- pairs. The bulk of the injected e^+e^- pairs can be accelerated to a relativistic velocity, and their kinetic energy is sufficient to power a superluminal radio blob observed in radio galaxies (see Figure 1). We also evaluate the detectability of X-ray flares during the reconnection event, and find that the future X-ray satellites will be able to detect the flares from Sgr A* and M87. We use the convention of $Q_x = Q/10^x$ throughout this Letter.

2. Physical Conditions in the Black Hole Magnetosphere

We consider a radio galaxy of SMBH mass $M = 10^9 M_9 M_\odot$ with a mass accretion rate of $\dot{M} = \dot{m}L_{\rm Edd}/c^2 \simeq 1.4 \times 10^{22} M_9 \dot{m}_{-4}$ g cm^{-2}, where c is the speed of light and $L_{\rm Edd}$ is the Eddington luminosity. The gravitational radius of the BH is $r_g = GM/c^2 \simeq 1.5 \times 10^{14} M_9$ cm. We consider that the accretion flow is in the MAD state, and then the magnetic field strength around the SMBH is estimated to be $B_{\rm mad} = \sqrt{\dot{M}c\Phi_{\rm mad}^2/(4\pi^2 r_g^2)}$ (e.g., Yuan & $\simeq 1.1 \times 10^3 M_9^{-1/2} \dot{m}_{-4}^{1/2} \Phi_{\rm mad,1.7}$ G Narayan 2014), where $\Phi_{\rm mad} \approx 50\Phi_{\rm mad,1.7}$ is the saturated magnetic flux (Tchekhovskoy et al. 2011; Narayan et al. 2012; McKinney et al. 2012; White et al. 2019). The high-resolution GRMHD simulation with a BH spin parameter $a = 0.9375$ suggests that magnetic reconnection occurs at a distance of $r_{\rm rec} \sim 2r_g$ (Ripperda et al. 2022). The value of $r_{\rm rec}$ could depend on a or other parameters, but we fix $r_{\rm rec} = 2r_g$ throughout this paper for simplicity. We estimate the reconnecting magnetic field strength to be (see Appendix A)

$$B_{\rm rec} \approx \sqrt{2} B_{\rm mad} \left(\frac{r_{\rm rec}}{r_g}\right)^{-2}$$
$$\simeq 3.9 \times 10^2 M_9^{-1/2} \dot{m}_{-4}^{1/2} \Phi_{\rm rec,1.2} \text{ G}, \tag{1}$$

where $\Phi_{\rm rec} = \sqrt{2}\Phi_{\rm mad}(r_{\rm rec}/r_g)^{-2}$ is the effective magnetic flux at the reconnection region. The magnetosphere will be formed around the SMBH. The minimum number density of the magnetosphere that can maintain the electric current for the BZ process is (Goldreich & Julian 1969; Levinson & Cerutti 2018)

$$n_{\rm GJ} = \frac{B_{\rm rec}\Omega_F}{2\pi ec} \approx \frac{B_{\rm rec}}{8\pi er_g}$$
$$\simeq 2.2 \times 10^{-4} M_9^{-3/2} \dot{m}_{-4}^{1/2} \Phi_{\rm rec,1.2} \text{ cm}^{-3}, \tag{2}$$

where $\Omega_F \approx ac/(4r_g)$ is the field line angular velocity (Tchekhovskoy et al. 2010; Nathanail & Contopoulos 2014; Ogihara et al. 2021; Camilloni et al. 2022) and we assume the BH spin parameter as $a \sim 1$. For the magnetosphere, which consists of e^+e^- pair plasma with the density $n_{\rm GJ}$, the magnetization parameter is

$$\sigma_{B,\rm GJ} = \frac{B_{\rm rec}^2}{4\pi n_{\rm GJ} m_e c^2} \approx 6.8 \times 10^{13} M_9^{1/2} \dot{m}_{-4}^{1/2} \Phi_{\rm rec,1.2}. \tag{3}$$

This value should be regarded as an upper limit, because the number density of the magnetosphere can be higher than $n_{\rm GJ}$. Various mechanisms of particle injection into the BH magnetosphere have been proposed (see Appendix B), which can lead to multiplicity of $\kappa_\pm \equiv n/n_{\rm GJ} \sim 1 - 10^3$. This results in the magnetization parameter of $\sigma_B \gtrsim 10^{10}$.

As for the reconnection region, where the accreting gas is being pushed out, GRMHD simulations imply that the possible range is $100 \ll \sigma_B \lesssim \sigma_{B,\rm GJ}$. In the following discussion, we assume σ_B is higher than the value of $\gamma_{e,\rm max}$ introduced below (Equation (4)).

3. Magnetic Reconnection in BH Magnetosphere

The relativistic magnetic reconnection accelerates nonthermal particles very efficiently (see Appendix C for a discussion).

If we ignore the effect of cooling, almost all the particles are accelerated up to the energy of $\gamma_e \sim \sigma_B$ (Guo et al. 2020). At the initial stage, the particles are accelerated by the reconnection electric field in a timescale of $t_{\rm acc} \approx \gamma_e m_e c/(e B_{\rm rec} \beta_{\rm rec})$, where $\beta_{\rm rec} \sim 0.1$ is the reconnection velocity in the kinetic domain (e.g., Guo et al. 2020). The accelerated electrons cool by the synchrotron emission with a timescale of $t_{\rm syn} = 6\pi m_e c/(\sigma_T B_{\rm rec}^2 \gamma_e)$. Equating the acceleration time and the cooling time, we obtain the maximum Lorentz factor as

$$\gamma_{e,\rm max} \approx \sqrt{\frac{6\pi e \beta_{\rm rec}}{\sigma_T B_{\rm rec}}} \simeq 1.9 \times 10^6 M_9^{1/4} \dot{m}_{-4}^{-1/4} \Phi_{\rm rec,1.2}^{-1/2} \beta_{\rm rec,-1}^{1/2}.$$
(4)

The synchrotron frequency for these electrons is

$$E_{\gamma,\rm max} = \frac{h e B_{\rm rec} \gamma_{e,\rm max}^2}{2\pi m_e c} = \frac{9 m_e c^2}{4\alpha_f} \beta_{\rm rec}$$
$$\simeq 16 \beta_{\rm rec,-1} \ {\rm MeV},$$
(5)

where h is the Planck constant and α_f is the fine structure constant. The value of $E_{\gamma,\rm max}$ depends only on $\beta_{\rm rec}$, whose value is almost constant according to recent PIC simulations.[7] The energy release rate by the reconnection event is estimated to be

$$L_{\rm rec} \approx 2 l_{\rm rec}^2 \frac{B_{\rm rec}^2}{8\pi} \beta_{\rm rec} c$$
$$\simeq 7.9 \times 10^{41} M_9 \dot{m}_{-4} f_l^2 \beta_{\rm rec,-1} \Phi_{\rm rec,1.2}^2 \ {\rm erg \ s^{-1}},$$
(6)

where $l_{\rm rec} = f_l r_g$ is the length scale of the reconnection region and f_l is a parameter. The duration of the reconnection event can be estimated to be

$$T_{\rm dur} \approx \frac{h_{\rm rec}}{2\beta_{\rm rec} c} \simeq 2.5 \times 10^4 M_9 \xi_{hl,-0.3} \beta_{\rm rec,-1}^{-1} \ {\rm s},$$
(7)

where $h_{\rm rec} = \xi_{hl} l_{\rm rec}$ is the thickness of the antiparallel magnetic fields that will reconnect during the reconnection event, and ξ_{hl} is a parameter. We consider that large-scale dynamics should determine $h_{\rm rec}$ and $l_{\rm rec}$, whereas microscopic plasma properties should determine the thickness of the reconnection layer where magnetic fields are dissipating. Since the system is in the fast cooling regime, all the released energy is converted to photons by synchrotron emission. We approximately suppose that the reconnection event injects monoenergetic particles at $\gamma_e \sim \gamma_{e,\rm max}$ and these particles are confined in magnetic islands. Then, we can write the broadband synchrotron photon spectrum as (e.g., Sari et al. 1998)

$$E_\gamma L_{E_\gamma} \approx L_{\rm rec} \left(\frac{E_\gamma}{E_{\gamma,\rm max}} \right)^{1/2}.$$
(8)

The power-law spectrum continues to the cooling frequency that is typically in radio bands. We should note that this photon spectrum is different from that obtained in 2D PIC simulations by Cerutti et al. (2013) and Hakobyan et al. (2019), whose

spectrum is extended beyond the burn-off limit (~ 160 MeV; see Appendix C for a discussion).

The photons in MeV energies interact with each other and create e^+e^- pairs. Using the photon spectrum of Equation (8), the optical depth for $\gamma\gamma$ interaction is estimated to be

$$\tau_{\gamma\gamma} \approx n_{\gamma_2} \sigma_{\gamma\gamma} l_{\rm rec} \simeq 1.2 \times 10^{-3} \dot{m}_{-4} f_l \beta_{\rm rec,-1} \Phi_{\rm rec,1.2}^2,$$
(9)

where n_{γ_2} is the number density of target photons (see Appendix D) and $\sigma_{\gamma\gamma} \approx f_{\gamma\gamma} \sigma_T$ is the approximated cross-section for two-photon interaction, σ_T is the Thomson cross-section, and $f_{\gamma\gamma} \sim 0.2$. Thus, the vast majority of the gamma rays escape from the system. Nevertheless, as shown in Appendix D, we find a high pair multiplicity as

$$\kappa_\pm = \frac{n_\pm}{n_{\rm GJ}} \approx \frac{4}{3} \alpha_f \tau_{\gamma\gamma} \sigma_{B,\rm GJ}$$
$$\simeq 7.7 \times 10^8 M_9^{1/2} \dot{m}_{-4}^{3/2} f_l \Phi_{\rm rec,1.2}^3 \beta_{\rm rec,-1}.$$
(10)

This mechanism can achieve several orders of magnitude higher values of multiplicity than those by the previously proposed scenarios. This is because the relativistic reconnection event can efficiently convert the magnetic energy into gamma rays of MeV energies in the compact region.

The leptons loaded into the pre-reconnection plasma change the magnetization parameter there, which affects the photon spectra and the pair production rate. In our fiducial parameters, the magnetization parameter after the lepton loading is estimated to be

$$\sigma_B = \frac{\sigma_{B,\rm GJ}}{\kappa_\pm} \simeq 8.7 \times 10^4 \dot{m}_{-4}^{-1} f_l^{-1} \Phi_{\rm rec,1.2}^{-2} \beta_{\rm rec,-1}^{-1}.$$
(11)

Then, e^+e^- pairs are accelerated up to $\gamma_e \sim \sigma_B$, and the flare spectrum has a cutoff at

$$E_{\gamma,\rm syn} = \frac{h e B_{\rm rec} \sigma_B^2}{2\pi m_e c}$$
$$\simeq 35 M_9^{-1/2} \dot{m}_{-4}^{-3/2} f_l^{-2} \Phi_{\rm rec,1.2}^{-3} \beta_{\rm rec,-1}^{-2} \ {\rm keV}.$$
(12)

Thus, the flare peak energy will significantly decrease after the lepton loading, which occurs around the light-crossing timescale, $l_{\rm rec}/c$. We refer to the spectral state with σ_B as the "low-energy flaring state" and that with $\sigma_{B,\rm GJ}$ as the "high-energy flaring state." Since the low-energy flaring state cannot produce MeV photons efficiently, the e^+e^- pairs are not produced.

The injected e^+e^- pairs in the pre-reconnection plasma rotate with an angular velocity of $\Omega_{\rm high} \sim \Omega_F \sim c/(4 r_g)$. On the other hand, according to GRMHD simulations (e.g., Narayan et al. 2012; McKinney et al. 2012), the plasma at midplane will have the angular velocity of $\Omega_{\rm mid} \sim \Omega_{\rm mad} \ll \Omega_K$, where $\Omega_{\rm mad}$ is the angular velocity in the MAD and $\Omega_K \simeq 0.26 c/r_g$ at $r \simeq 2 r_g$ is the Keplerian angular velocity. Thus, $\Omega_{\rm mid} \ll \Omega_{\rm high}$ should be satisfied, and the injected e^+e^- pairs will escape in a streaming timescale of $\sim 2 l_{\rm rec}/c$. This timescale is shorter than the duration of the reconnection event, $T_{\rm dur}$. Hence, after the streaming escape timescale, the reconnection event will become able to accelerate electrons up to $\gamma_{e,\rm max}$ again, leading to efficient MeV gamma-ray production. These gamma rays will produce the copious e^+e^- pairs again, and thus, we expect oscillation between the low- and high-energy flaring states. The timescale of pair production and streaming escape is

---

[7] The value of $\beta_{\rm rec}$ is almost constant in time for each PIC simulation, and the variation among the different PIC simulations are also small (e.g., Guo et al. 2020)
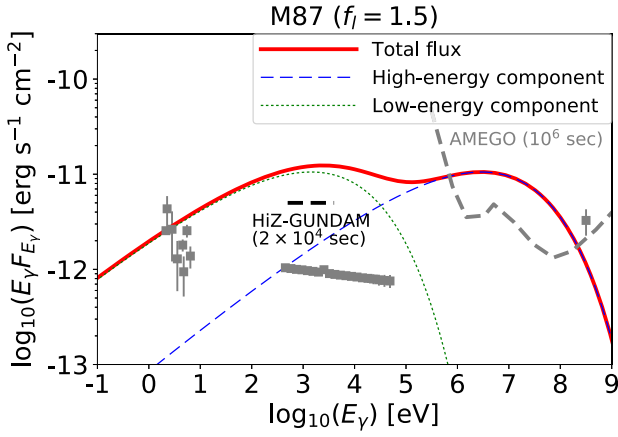
Figure 2. Photon spectrum of a reconnection-driven flare from M87. Parameters are $M = 6.3 \times 10^9 M_\odot$, $\dot{m} = 5 \times 10^{-5}$, $f_l = 1.5$, and $\xi_{hl} = 0.5$. The blue-dashed, green-dotted, and red-solid lines are for the high-energy flaring state, the low-energy flaring state, and their sum, respectively. The data points are obtained from Table A8 in EHT MWL Science Working Group et al. (2021), which is in the quiescent state. Our model predicts flares of ∼10 times higher luminosity. The black- and gray-dotted lines are sensitivity curves for HiZ-GUNDAM (2×10^4 s: Yonetoku et al. 2020) and AMEGO (10^6 s: McEnery et al. 2019), respectively.

comparable, and thus, we consider that the duration for each state should be similar.

To discuss observational signature, we numerically calculate the photon spectra by a reconnection event. We solve the transport equation for the nonthermal leptons accelerated by the reconnection and calculate the synchrotron photon spectrum (see, e.g., Kimura et al. 2020, for technical details). The BH mass and mass accretion rate for M87 can be estimated by other studies (e.g., Event Horizon Telescope Collaboration et al. 2019c; Kimura & Toma 2020), and we can regard β_{rec} and Φ_{rec} as constants, based on relativistic PIC simulations (Guo et al. 2020) and GRMHD simulations (Narayan et al. 2012; Ripperda et al. 2022), respectively. Then, f_l and ξ_{hl} are the only free parameters in our scenario. We choose $f_l = 1.5$ and $\xi_{hl} = 0.5$ so that the pair plasma loaded in the magnetosphere can power the observed radio blobs (see Section 4). We cannot explain the power of radio blobs with a smaller value of f_l.

Figure 2 shows the resulting spectra with a parameter set for M87, where we average over the flux from each state. Our model predicts a broadband flare whose flux in X-ray bands is about 10 times higher than that for the quiescent state. The core of M87 exhibited such a high flux state in the past (e.g., Abramowski et al. 2012). Based on the high-resolution GRMHD simulation (Ripperda et al. 2022), the magnetic reconnection repeatedly occurs in a timescale of $T_{int} \sim 2000 r_g/c \sim 2$ yr. On the other hand, the duration of the flare is very short, $T_{dur} \sim 3$ days (see Table 1). Thus, we need to monitor M87 for years with a cadence of less than a few days. We cannot occupy high-sensitivity pointing facilities, e.g., Chandra, for such a long time. Thus, we need to rely on all-sky X-ray monitors, such as Swift-BAT (Barthelmy et al. 2005) and MAXI (Matsuoka et al. 2009). Although the predicted flux is much lower than the sensitivities for current X-ray monitors, future X-ray monitors, such as HiZ-GUNDAM (Yonetoku et al. 2020) and the Einstein Probe (Yuan et al. 2015), can detect the X-ray flares. The timescale of the oscillation between the low- and high-energy flaring states is $2l_{rec}/c \simeq 93$ ks, which is longer than the integration time required for detection by

HiZ-GUNDAM (see Figure 2). Also, future X-ray satellite networks might enable the sensitive pointing X-ray telescopes to follow up the flare event within an hour. Then, we will be able to observe the oscillation between the low- and high-energy flaring states, which will enable us to determine the values of f_l and ξ_{hl}. Therefore, our scenario will be robustly tested by future X-ray observations.

4. Origin of Superluminal Radio Blobs

The e^+e^- pairs injected in the magnetosphere can lose energies by synchrotron radiation, but they may be heated up by the synchrotron self-absorption (SSA) process. As shown in Appendix E, the leptons are easily thermalized in typical radio galaxies. At the time of lepton loading, we can write the spectrum of the e^+e^- pairs as a power law with an index of $s \sim 1$, i.e., $N_{E_\pm} \propto E_\pm^{-1}$, where $E_\pm$ is the energy of the e^+e^- pairs. This is a good approximation if the parent photon spectrum is a power law (see Appendix D). Considering the number and energy conservations during the thermalization, we obtain

$$k_B T_\pm \approx \frac{E_{\pm,max}}{3 \ln(E_{\pm,max}/E_{\pm,min})} \sim 0.96 \beta_{rec,-1} \, \text{MeV}, \quad (13)$$

where $E_{\pm,max} \approx E_{\gamma,max}/2$ and $E_{\pm,min} \sim m_e c^2$ are the maximum and minimum energies of the e^+e^- pairs, respectively. The mean energy of the thermalized e^+e^- pairs is $3k_B T_\pm \simeq 2.9 \beta_{rec,-1}$ MeV, and thus, we can regard this as a relativistic plasma. Such a hot gas can accelerate to relativistic speed by its adiabatic expansion.

The thermalized pairs do not cool via the synchrotron process in the initial phase. We can write the synchrotron peak frequency for thermal plasma as $\nu_{blb,syn} \simeq 9\theta_\pm^2 e B_{blb}/(2\pi m_e c)$ and the emissivity at $\nu = \nu_{blb,syn}$ as $j_\nu = 3\sigma_T c \theta_\pm^2 B_{blb}^2 n_{blb}/(2\pi \nu_{blb,syn})$, where B_{blb} and n_{blb} are the magnetic field strength and the number density of the blob and $\theta_\pm = k_B T_\pm/(m_e c^2)$. The optical depth at the synchrotron peak can roughly be estimated to be

$$\tau_{ssa,blb} \approx \frac{j_\nu c^2 R}{2\nu_{blb,syn}^2 k_B T_\pm} \approx \frac{16\pi^3}{3^6} \frac{e}{B_{blb}\theta_{blb}^5} n_{blb} R$$
$$\simeq 9.0 \times 10^5 M_9^{1/2} \dot{m}_{-4}^{3/2} f_l^2 \Phi_{rec,1.2}^3 \beta_{rec,-1}^{-4}, \quad (14)$$

where we use the values immediately after the lepton injection with $R \sim f_l r_g$ in the estimate. The thermal plasma cannot cool by the synchrotron process while $\tau_{ssa,blb} > 1$. The total energy of the lepton plasma during the reconnection event is estimated to be

$$\mathcal{E}_{blb} \approx \dot{N}_{\gamma\gamma} T_{dur} E_{\pm,max}$$
$$\simeq 1.1 \times 10^{43} M_9^2 \dot{m}_{-4}^2 f_l^4 \xi_{hl,-0.3} \beta_{rec,-1} \Phi_{rec,1.2}^2 \, \text{erg}. \quad (15)$$

Theoretically, it is unknown how such a nonsteady, nonaxisymmetric MHD flow accelerates, whereas steady, axisymmetric MHD acceleration of hot flows was extensively studied with possible cooling effects (Vlahakis & Königl 2003; Komissarov et al. 2009; Tanaka & Toma 2020). According to VLBI observations, the blob velocities are widely distributed for $\beta \lesssim 0.7$ at $R \sim 100$–$1000 r_g$ (Nakamura et al. 2018; Park et al. 2019). The injected energy can be dissipated by internal shocks (Komissarov 2012) or plasma kinetic instabilities (e.g.,

Table 1
Resulting Physical Quantities in M87 and Sgr A*

Name	$B_{\rm rec}$ (G)	$\log_{10}(n_{\rm GJ})$ (cm^{-3})	$\log_{10}(\sigma_{B,\rm GJ})$	$\log_{10}(L_{\rm rec})$ (erg s^{-1})	$\log_{10}(T_{\rm dur})$ (s)	$\log_{10}(\kappa_{\pm})$	$F_{\rm radio}$ (43 GHz) (mJy)
M87	1.1×10^2	-5.0	14.1	42.8	5.4	9.0	12
Sgr A*	4.8×10^2	-1.2	11.5	36.8	1.8	4.1	0.07

Note. We use $f_l = 1.5$ for M87, $f_l = 0.6$ for Sgr A*, and $\xi_{hl} = 0.5$ for both objects. We use $M = 6.3 \times 10^9 M_\odot$, $\dot{m} = 5 \times 10^{-5}$, and $d_L = 17$ Mpc for M87 (Event Horizon Telescope Collaboration et al. 2019b; Kimura & Toma 2020) and $M = 4.0 \times 10^6 M_\odot$, $\dot{m} = 6 \times 10^{-7}$, and $d_L = 8$ kpc for Sgr A* (Event Horizon Telescope Collaboration et al. 2022a; Kuze et al. 2022).

Sironi et al. 2021; Kawashima et al. 2022), which leads to nonthermal lepton acceleration. These leptons emit radio signals where $\tau_{\rm ssa,blb} < 1$, and we observe it as a radio blob. The radio luminosity and flux from the blob can be estimated to be

$$L_{\rm radio} \approx \frac{\mathcal{E}_{\rm blb}}{R_{\rm dis}/c} \simeq 2.3 \times 10^{37} M_9 \dot{m}_{-4}^2 f_l^4$$
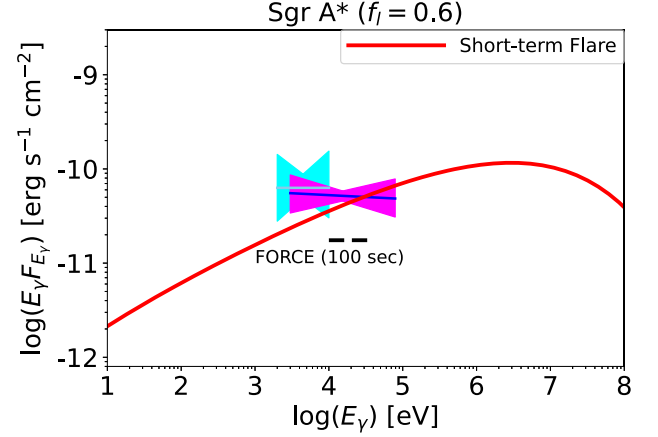$$\times \xi_{hl,-0.3} \beta_{\rm rec,-1} \Phi_{\rm rec,1.2}^2 \mathcal{R}_2^{-1} \text{ erg s}^{-1}, \quad (16)$$

$$F_{\rm radio} \sim \frac{L_{\rm radio}}{4\pi d_L^2 \nu_{\rm blob}}, \quad (17)$$

where $R_{\rm dis} = \mathcal{R} r_g$ is the dissipation radius, $\mathcal{R}$ is a parameter, and $\nu_{\rm blob}$ is the radio frequency. The value of $F_{\rm radio}$ for M87 is shown in Table 1. VLBI observations detect radio blobs of $F_{\rm radio} \sim 10$ mJy at $R \sim 100$–$1000 r_g$ in M87 (Hada et al. 2013; Walker et al. 2018; Park et al. 2019), which is in rough agreement with our prediction. The injection and expansion of pairs are concentrated on the edge of the magnetosphere, which may also be compatible with the limb-brightened feature of the jet (see Kim et al. 2018; Takahashi et al. 2018).

5. Application to Sgr A*

Recent studies suggest that Sgr A* likely has an MAD. Large-scale GRMHD simulations revealed that accretion by the Wolf–Rayet wind leads to a formation of an MAD around Sgr A* (Ressler et al. 2020), which is consistent with the variability of Sgr A* (Murchikova et al. 2022). Sgr A* is known as a very low accretor, which likely leads to an MAD state owing to a rapid advection of large-scale magnetic fields (Cao 2011; Kimura et al. 2021b). Recent radio imaging of the horizon scale also favors a relatively face-on MAD state in Sgr A* (Event Horizon Telescope Collaboration et al. 2022b), although models with SANE-mode RIAFs are not ruled out.

We apply our scenario to Sgr A*, tabulate resulting physical quantities in Table 1, and show the resulting flare spectrum in Figure 3. Here, we use $f_l = 0.6$ and $\xi_{hl} = 0.5$ so that the resulting X-ray flux is consistent with the observed X-ray flux for Sgr A* flares (e.g., Nowak et al. 2012; Neilsen et al. 2013; Barrière et al. 2014).[8] Owing to the low lepton loading rate, Sgr A* can maintain a high magnetization even after the lepton loading (see Equation (11)), which causes the reconnection flare for Sgr A* to exhibit only the high-energy state. The near-infrared (NIR) flux by our scenario is comparable to that observed in the quiescent state. The duration of the

---

[8] The value of f_l for Sgr A* can be different from that for M87, because the large-scale magnetic field configuration may be different. Sgr A* may accrete mass from the Wolf–Rayet winds (Ressler et al. 2020), whereas M87 is expected to accrete mass from the interstellar medium.

Figure 3. Photon spectrum of a reconnection-driven flare from Sgr A* (solid red line). Parameters are $M = 4.0 \times 10^6 M_\odot$, $\dot{m} = 6 \times 10^{-7}$, $f_l = 0.6$, and $\xi_{hl} = 0.5$. The X-ray flare data (cyan and magenta regions) are taken from Nowak et al. (2012) and Barrière et al. (2014), respectively. The black-dashed line is the sensitivity curve for FORCE (100 s: Nakazawa et al. 2018).

reconnection-driven flare is around $T_{\rm dur} \sim 10^2$ s, which is shorter than the time bin for the current flare analyses for Sgr A*, $\Delta t \sim 300$ s (e.g., Neilsen et al. 2013). Nowak et al. (2012) and Barrière et al. (2014) reported a substructure of ~ 100 s duration in the lightcurve of bright X-ray flares, which may be caused by the reconnection-driven flare. We need more statistics to confirm this feature, and the future hard X-ray satellite, FORCE (Nakazawa et al. 2018), will be able to observe a rapid variability with high statistics.

Our model predicts that Sgr A* may have radio blobs at $R \sim 100$–$1000 r_g$, but the radio flux from Sgr A* is too faint to clearly detect with current facilities. Figure 4 shows $L_{\rm radio}$ as a function of M and $\dot{m}$, where we see $L_{\rm radio}$ strongly depends on M and $\dot{m}$ (see Appendix E for the method for estimating $\mathcal{E}_{\rm blb}$; see also Equation (16)). We find that $F_{\rm radio}$ for Sgr A* is ~ 0.1 mJy, which may be challenging to detect. VLBI images on Sgr A* are likely affected by the refractive scattering effect in the foreground plasma, which effectively adds 1–10 mJy noises to the data (Cho et al. 2022). Brinkerink et al. (2019) reported a possible blob-like feature in their 86 GHz VLBI Sgr A* image with a flux density of ~ 10 mJy. However, it is again still unclear whether this substructure is intrinsic to Sgr A* or caused by the scattering effect. Higher sensitivity and dedicated monitoring observations would be demanded to firmly detect radio blobs around Sgr A*.

The observed duration of Sgr A* X-ray flares is $\sim 10^3$–10^4 s, and the observed flare rate is about ~ 0.1–0.3 day^{-1} for the ones as bright as in Figure 3 (Degenaar et al. 2013; Neilsen et al. 2013). Our scenario predicts a shorter flare duration of $T_{\rm dur} \sim 10^2$ s and a higher flare rate of ~ 1–2 day^{-1}. Thus, our
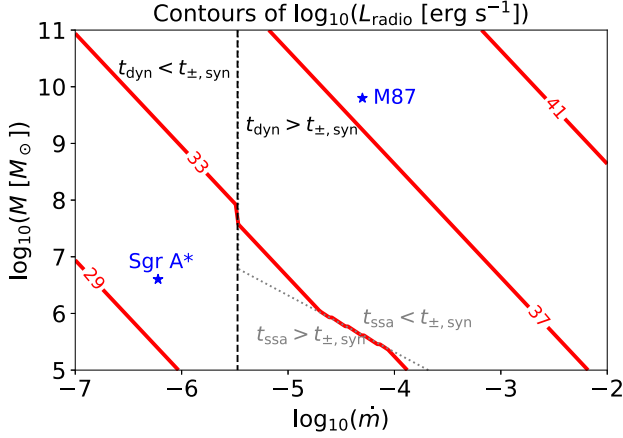
Figure 4. Contours of radio luminosity as a function of M and $\dot{m}$ with $f_l = 1.0$ and $\xi_{hl} = 0.5$. The red lines show the contours of $\log_{10}(L_{\mathrm{radio}})$ in cgs unit. The dotted gray line shows $t_{\mathrm{ssa}} = t_{\pm,\mathrm{syn}}$, and the dashed black line shows $t_{\mathrm{dyn}} = t_{\pm,\mathrm{syn}}$. The blue stars show the parameters for Sgr A* and M87.

scenario cannot explain the typical timescales of the observed X-ray flares.[9] Nevertheless, our scenario could reconcile with the observed flare properties. The magnetic reconnection in the magnetosphere should produce bipolar outflows, one of which collides with the dense plasma in an MAD (Ripperda et al. 2022). This collision triggers another magnetic reconnection event at $R \sim 5$–$30 r_g$, which will produce a flare with longer duration (Dexter et al. 2020; Porth et al. 2021; Scepi et al. 2022). Also, in Sgr A*, the wind-fed accretion leads to a weaker variability (Murchikova et al. 2022). This could be caused by a weaker turbulent field in the wind-fed accretion flow, which implies that development of Rayleigh–Taylor instability likely takes more time than a typical AGN that accretes turbulent fields from the outer accretion disk. This would lead to a longer interval between the reconnection events, which alleviates the tension of the flaring rate.

Sgr A* exhibits strong flares in the NIR band, and they may be powered by thermal electrons heated by the magnetic reconnection in the magnetically dominated regions in the MAD (Dexter et al. 2020; Scepi et al. 2022). In our scenario, a large number of e^+e^- pairs are injected into the magnetosphere, and they emit submillimeter emission via synchrotron at $R \sim 1$–$10 r_g$, as the e^+e^- plasma in Sgr A* is SSA thin. They would emit NIR photons if they were additionally heated by some mechanism. However, the number density of the e^+e^- pairs in the magnetosphere ($n_{\mathrm{GJ}} \sim 0.06\,\mathrm{cm}^{-3}$) is much lower than that in the surrounding accretion flow. Even after the pair injection, the magnetization parameter is $\sigma_B > 10^7$, which is much higher than that investigated by GRMHD simulations ($\sigma_B \sim 10^2$, see, e.g., Scepi et al. 2022). Thus, it is unlikely that the injected e^+e^- pairs power the NIR flares in Sgr A*. Gravity Collaboration et al. (2018) reported orbital motions of bright spots in NIR flares. These may be caused by outflows interacting with the surrounding accretion flow (Matsumoto et al. 2020). The reconnection in the BH magnetosphere can potentially trigger the NIR flares by providing outflows.

---

[9] We should note that the energy of the individual e^+e^- particles injected by $\gamma\gamma$ pair production is too low to emit X-rays, and thus, the newly injected e^+e^- pairs cannot explain X-ray flares in Sgr A*, either.

6. Summary

We have examined magnetic reconnection in the BH magnetosphere and subsequent nonthermal particle production as a lepton loading mechanism to AGN jets. The extremely high-resolution GRMHD simulation by Ripperda et al. (2022) suggested that magnetic reconnection repeatedly occurs in a magnetically dominated part of the equatorial disk near the BH horizon. The magnetic energy is efficiently converted to the energy of nonthermal electrons, which subsequently cool by MeV gamma-ray flares. These gamma rays interact with each other and produce copious e^+e^- pairs. We have evaluated the amount of e^+e^- pairs and found that the plasma density around the reconnection region can be $\sim 10^9$ times higher than the Goldreich–Julian density for a typical radio galaxy, which is sufficient for explaining signals from radio jets. The injected e^+e^- pairs are optically thick for the SSA process, and thus, the e^+e^- plasma stores all the injected energy that is enough to power the observed superluminal radio blobs in M87. Our scenario predicts that radio blobs may exist around Sgr A* if it has an MAD, but they are faint and consistent with no clear detection by current facilities. In our scenario, the reconnection event inevitably produces X-ray signals detectable by future X-ray satellites, such as HiZ-GUNDAM and FORCE, which will provide a concrete test for our scenario.

Appendix A
Magnetic Field Structure in the BH Magnetosphere

We estimate the structure of the magnetic field in the BZ process. We use the Boyer–Lindquist coordinates (t, φ, r, θ) and the unit of $GM = 1$ and $c = 1$ (and thus $r_g = 1$) in this appendix. The metric of Kerr spacetime can be written as
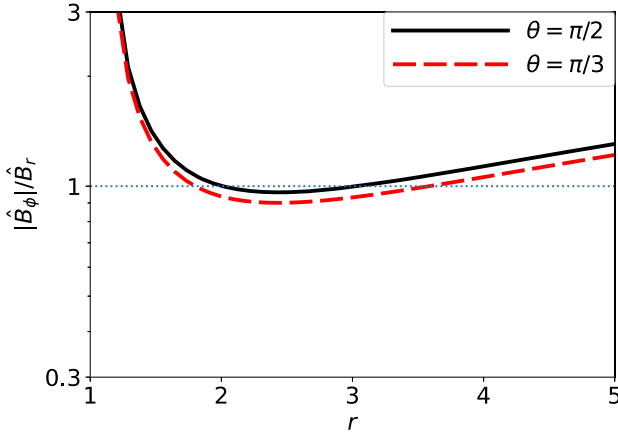
$$ds^2 = -\alpha^2 dt^2 + \gamma_{ij}(\beta^i dt + dx^i)(\beta^j dt + dx^j), \quad (A1)$$

where the nonzero components are $\alpha = \sqrt{\varrho^2 \Delta / \Sigma}$, $\beta^\varphi = -2ar/\Sigma$, $\gamma_{\varphi\varphi} = \Sigma \sin^2\theta / \varrho^2$, $\gamma_{rr} = \varrho^2/\Delta$, and $\gamma_{\theta\theta} = \varrho^2$. Here, we have defined $\varrho^2 = r^2 + a^2\cos^2\theta$, $\Delta = r^2 + a^2 - 2r$, and $\Sigma = (r^2 + a^2)^2 - a^2\Delta\sin^2\theta$. The fiducial observers (FIDOs), whose world lines are perpendicular to the hypersurface of $t = $ const., are described by the coordinate four-velocity $n^\mu = (1/\alpha, -\beta^\varphi/\alpha, 0, 0)$. FIDOs rotate with coordinate angular velocity $\Omega = d\varphi/dt = -\beta^\varphi$. Maxwell equations in this 3+1 formalism can be reduced to Komissarov (2004)

$$\partial_t \boldsymbol{B} + \nabla \times \boldsymbol{E} = 0, \quad -\partial_t \boldsymbol{D} + \nabla \times \boldsymbol{H} = 4\pi \boldsymbol{J}, \quad (A2)$$

$\nabla \cdot \boldsymbol{B} = 0$, and $\nabla \cdot \boldsymbol{D} = 4\pi\rho$. $\boldsymbol{D}$ and $\boldsymbol{B}$ are the electric and magnetic fields measured by FIDOs, while $\boldsymbol{E}$ and $\boldsymbol{H}$ are those in the coordinate basis, and they have relations

$$\boldsymbol{E} = \alpha \boldsymbol{D} + \boldsymbol{\beta} \times \boldsymbol{B}, \quad \boldsymbol{H} = \alpha \boldsymbol{B} - \boldsymbol{\beta} \times \boldsymbol{D}. \quad (A3)$$

Figure 5. The ratio of toroidal to poloidal magnetic fields measured by FIDOs in the Boyer–Lindquist coordinates as a function of the distance from the BH horizon.

In the following, we estimate the ratio of $\hat{B}_r = \sqrt{\gamma_{rr}}B^r$ and $\hat{B}_\varphi = B_\varphi \big/ \sqrt{\gamma_{\varphi\varphi}}$, which are the radial and toroidal magnetic field components with respect of the orthonormal basis carried by FIDOs.

The high-resolution GRMHD simulation (Ripperda et al. 2022) shows that the accretion disk in the MAD state is so thin that the poloidal magnetic field in the BH magnetosphere has a monopole shape at $r \lesssim 5r_g$, i.e., $\sqrt{\gamma}B^r = $ const. The force-free condition is a good approximation between the outer and inner light surfaces in the BH magnetosphere. Then, for the steady, axisymmetric state, the above Maxwell equations lead to $\boldsymbol{B} \cdot \nabla H_\varphi = 0$, i.e., $H_\varphi = \alpha B_\varphi = $ const. along a magnetic field line (Komissarov 2004; Toma & Takahara 2016). Therefore, we have

$$\frac{|\hat{B}_\varphi|}{\hat{B}_r} \propto \frac{\sqrt{\gamma_{\theta\theta}}}{\alpha} \qquad (A4)$$

for a fixed θ. Analyses of the special relativistic MHD outflows with high σ (Beskin 2010; Toma & Takahara 2013) indicate that

$$\hat{B}_\varphi \sim -\hat{B}_r, \quad \text{at } r \sim r_{\text{ols}}, \qquad (A5)$$

where r_{ols} means the radius of the outer light surface. Then we can plot $|\hat{B}_\varphi|/\hat{B}_r$ as shown in Figure 5. Here we have assumed $a \sim 1$. The outer and inner light surfaces are located at $r \simeq 1.4$ and 3.0, respectively, for $\theta = \pi/2$. In the region between the two light surfaces, which we are interested in, one has $|\hat{B}_\varphi| \sim \hat{B}_r$, and the magnetic field strength at the reconnection point can be estimated by Equation (1).

Appendix B
Lepton Loading Mechanisms

Several mechanisms of lepton loading into AGN jets have been studied. Pair production by Comptonized MeV photons from hot accretion flows has been discussed for a long time (e.g., Levinson & Rieger 2011; Mościbrodzka et al. 2011; Wong et al. 2021), and this process may achieve $\kappa_\pm \sim 1$–100 for parameters of M87. Hot accretion flows in the MAD state may efficiently accelerate nonthermal particles by magnetic reconnection, which leads to GeV gamma-ray production (Kimura & Toma 2020; Kuze et al. 2022). Since optical depth

for $\gamma\gamma$ interactions for GeV gamma rays is higher than that for MeV gamma rays, this process can enhance the pair production rate at the magnetosphere, compared to the case only considering MeV gamma rays. These mechanisms can efficiently create e^+e^- pairs when the accretion rate is high. However, the estimated multiplicity is ~ 100–10^3, which is still lower than the required multiplicity estimated by radio observations ($\kappa_\pm \gtrsim 10^5$; see, e.g., Kino et al. 2015).

Nonthermal hadronic particles, such as protons, neutrons, and atomic nuclei, may be loaded if hot accretion flows accelerate cosmic rays (Toma & Takahara 2012; Kimura et al. 2014, 2015), but with the parameter set for M87, this process cannot achieve the multiplicity required by the radio observations.

Particle acceleration in the vacuum gap is also discussed as a lepton loading mechanism. Broderick & Tchekhovskoy (2015) argued that the multiplicity around the gap can be as high as ~ 100, and it may further be enhanced to $\kappa_\pm \sim 10^5$ at the far downstream of the jet. However, GR PIC simulations by Kisaka et al. (2020) found that the pair multiplicity around the gap is $\kappa_\pm \sim 1$, and they also showed that $\kappa_\pm$ may not be so high even at the far downstream.

Compared to these mechanisms, magnetic reconnection in the BH magnetosphere can achieve many orders of magnitude higher multiplicity because of the efficient, local conversion of magnetic energy into MeV photon energy. In our scenario, high-density e^+e^- pairs are intermittently loaded into the limited region in BH magnetosphere, and thus, the quiescent state or the other part of the BH magnetosphere could have the vacuum gap, which may produce very-high-energy gamma rays (Kisaka et al. 2022).

Appendix C
Particle Acceleration by Relativistic Magnetic Reconnections

Many PIC simulations show that relativistic reconnection very efficiently accelerates nonthermal particles, although the details of the mechanism are still controversial. As a pioneering work, Zenitani & Hoshino (2001) showed that using 2D PIC simulations, the reconnection electric field generated at the X-point accelerates particles very rapidly with a timescale of $t_{\text{acc}} \approx \gamma_e m_e c/(eB\beta_{\text{rec}})$. We use this timescale as the fiducial model, as this is a simple and robust mechanism.

PIC simulations with larger box sizes and longer durations have been available since 2010 s. Guo et al. (2014) revealed that the X-point acceleration is subdominant, and Fermi-like acceleration is essential using a set of 2D PIC simulations. The acceleration timescale can be represented by $t_{\text{acc,G14}} \approx (\sigma_B/10)^{-1/2}l_{\text{rec}}/c$, where l_{rec} is the size of the reconnecting magnetic field. Guo et al. (2021) reached similar conclusions with 3D simulations with various parameter sets. However, this acceleration timescale is not applicable to our scenario. For the Fermi-type acceleration to work effectively, the gyration timescale, $t_L \approx E_e/(eBc)$, needs to be shorter than the acceleration timescale, whereas $t_{\text{acc,G14}} \ll t_L$ is satisfied for typical parameters used in our calculations. More recently, Sironi (2022) revealed that the electric fields at the X-point play an essential role in the initial phase of the particle acceleration, and thus, our treatment focusing on the X-point acceleration is reasonable.

Zhang et al. (2021) argued that the particle acceleration mainly occurs by the electric fields at X-points. In 3D

simulations, the reconnection dynamics is turbulent. Energetic particles are not trapped in magnetic islands, and some of them continuously gain energy from the X-point electric fields. This mechanism works for particles of $\gamma_e \gtrsim 3\sigma_B$, but the lower-energy particles should be confined in the magnetic islands even in 3D simulations. Since our scenario focuses on particles of $\gamma_e \ll \sigma_B$, their model is inappropriate to our scenario.

Comisso & Sironi (2018; 2019) showed that the reconnection acceleration by the turbulent medium leads to anisotropic pitch angle distribution. This is caused by the strong guide fields at the reconnection points due to the turbulent nature. In this case, the synchrotron emission is suppressed, and particles may be accelerated to higher energies than that for the isotropic distribution. Then, we expect gamma rays of energies higher than that given in Equation (5). Nevertheless, Ripperda et al. (2022) found that the magnetic reconnection in the BH magnetosphere proceeds with almost no guide field, which is assumed in our scenario. We speculate that some different initial magnetic field configuration may lead to magnetic reconnection with a strong guide field, as seen in Ball et al. (2018), which may lead to production of higher energy gamma rays.

Cerutti et al. (2013) performed a set of reconnection simulations with the effect of synchrotron radiation feedback. They found that some fraction of electrons can achieve energies higher than that given by Equation (4), because the magnetic field at the X-point is much weaker than the upstream plasma. These high-energy electrons lead to the photon spectrum with a high-energy tail above the burn-off limit (∼160 MeV). However, the emerging photons above the burn-off limit are subdominant in terms of the luminosity and the number density. Also, the high-energy photons above 160 MeV are strongly beamed to the direction of the reconnecting magnetic field lines, which will significantly reduce the pair production rate. For these reasons, we concentrate on the pair production and emerging spectra for the lower-energy photons in this Letter.

Hakobyan et al. (2019) performed a set of reconnection simulations taking into account the synchrotron energy loss and e^+e^- pair production. Their simulations also exhibit the production of gamma rays of energies higher than that given in Equation (5). However, they performed only 2D simulations, and it is unclear how 3D effects will modify the emerging photon spectra.

Sridhar et al. (2021; 2022) performed 2D PIC simulations taking account of the Compton cooling. Their results show that spectra for nonthermal particles are steeper for the cases with stronger cooling, which might indicate that the gamma-ray emission could be suppressed if the cooling is efficient. Nevertheless, the Compton cooling is different from the synchrotron cooling: the Compton cooling is efficient for electrons of any pitch angle and position, whereas the synchrotron emission more efficiently cools electrons with larger pitch angles and at regions of stronger magnetic fields.

Appendix D
Pair Production Rate and Multiplicity

The pair production rate is estimated to be

$$\dot{N}_{\gamma\gamma} = 2 \int n_{\gamma_1} n_{\gamma_2} \sigma_{\gamma\gamma} c \, dV, \tag{D1}$$

where n_{γ_1} and n_{γ_2} are the number density of interacting photons, $\sigma_{\gamma\gamma}$ is the cross-section, and dV is the volume of the interacting region. Here, we consider a uniform emission region and $\gamma\gamma$ interactions inside the sphere of size $l_{\rm rec}$. The photons of $E_{\gamma,\max}$ mainly interact with the photons of $E_{\gamma_2} \approx (2m_e c^2)^2/E_{\gamma,\max}$, whose number density can be

$$n_{\gamma_2} \approx \frac{L_{\rm rec}(E_{\gamma_2}/E_{\gamma,\max})^{1/2}}{4\pi l_{\rm rec}^2 c E_{\gamma_2}} \approx \frac{L_{\rm rec}}{8\pi l_{\rm rec}^2 m_e c^3}. \tag{D2}$$

The optical depth for the $\gamma\gamma$ interaction is then given by Equation (9). Then the pair production rate can be approximated to be

$$\dot{N}_{\gamma\gamma} \approx \frac{L_{\rm rec}\tau_{\gamma\gamma}}{E_{\gamma,\max}}. \tag{D3}$$

The number density of the e^+e^- pairs can be written as (e.g., Kimura & Toma 2020)

$$n_{\pm} \approx \frac{3\dot{N}_{\gamma\gamma}}{l_{\rm rec}^2 c}. \tag{D4}$$

Using Equations (3), (6), (9), (D3), and (D4), we obtain Equation (10).

We can approximately write the injection spectrum of the e^+e^- pairs as $\dot{N}_{E_\pm,\rm inj} \propto E_\gamma^{-1}$. Suppose that the photon spectrum is a power-law form, $E_\gamma n_{E_\gamma} \approx n_0(E_\gamma/E_{\gamma,\max})^s$, where n_0 is a normalization factor. A photon of $E_{\gamma,1}$ interact with photons of $E_{\gamma,2} \approx (2m_e c^2)^2/E_{\gamma,1}$. The number density of these photons is given by

$$n_{\gamma,1} \approx n_0\left(\frac{E_{\gamma,1}}{E_{\gamma,\max}}\right)^s, \tag{D5}$$

$$n_{\gamma,2} \approx n_0\left(\frac{4m_e^2 c^4}{E_{\gamma,1}E_{\gamma,\max}}\right)^s. \tag{D6}$$

We approximate $\sigma_{\gamma\gamma}$ as a delta function, and the mean energy of the e^+e^- pair produced by photons of E_γ is $E_\pm \approx E_\gamma/2$. Then, the spectrum of the e^+e^- pairs can be given by

$$\begin{aligned} E_\pm \dot{N}_{E_\pm,\rm inj} &\approx 2cf_{\gamma\gamma}\sigma_T n_{\gamma,1} n_{\gamma,2} V \\ &\approx 2cf_{\gamma\gamma}\sigma_T n_0^2 V\left(\frac{2m_e c^2}{E_{\gamma,\max}}\right)^{2s}, \end{aligned} \tag{D7}$$

where V is the volume of the injection region. This does not depend on $E_{\gamma,1}$, so we can write $\dot{N}_{\pm,\rm inj} \propto E_\pm^{-1}$.

Appendix E
Energy Loss in the Lepton Plasma

The SSA heating timescale is written as (e.g., Asano & Mészáros 2011)

$$t_{\rm ssa} = \frac{\gamma_\pm m_e c^2}{\int dE_\gamma E_\gamma n_{E_\gamma} \sigma_{\rm ssa} c}, \tag{E1}$$

where n_{E_γ} is the differential photon number density, $\gamma_\pm = E_\pm/(m_e c^2)$, and $\sigma_{\rm ssa}$ is the SSA cross-section (Ghisellini & Svensson 1991). With the hard lepton injection spectrum of $dN/dE_\pm \propto E_\pm^{-1}$, the synchrotron spectrum is dominated by the photons produced by the highest energy leptons. The SSA

heating rate by the lowest energy photons of $\nu_{\min} = eB_{\rm rec}/(2\pi m_e c \gamma_{\pm,\max})$ is dominant, which allows us to write

$$\int dE_\gamma E_\gamma n_{E_\gamma} \sigma_{\rm ssa}$$

$$\approx \frac{\dot{N}_{\gamma\gamma} E_{\pm,\max}}{4\pi l_{\rm rec}^2 c} \min\left(\frac{t_{\rm dyn}}{t_{\pm,\rm syn}},\ 1\right)\left(\frac{\nu_{\min}}{\nu_{\max}}\right)^{4/3} \sigma_{\rm ssa0}, \qquad \text{(E2)}$$

where

$$\sigma_{\rm ssa0} \approx \frac{2^{11/3} 3^{7/6} \pi^2 \Gamma^2(4/3)}{5} \frac{e}{B_{\rm rec}}, \qquad \text{(E3)}$$

$\nu_{\min} = eB_{\rm rec}/(2\pi \gamma_{\pm,\max} m_e c)$ and $\nu_{\max} = eB_{\rm rec}\gamma_{\pm,\max}^2/(2\pi m_e c)$, $\Gamma(x)$ is the Gamma function, $t_{\rm dyn} = R_{\rm rec}/c$ is the dynamical timescale, and $t_{\pm,\rm syn}$ is the synchrotron cooling timescale. For our reference parameter set, we obtain

$$t_{\rm ssa} \approx \frac{4\pi l_{\rm rec}^2}{\dot{N}_{\gamma\gamma}\sigma_{\rm ssa0}}\left(\frac{\nu_{min}}{\nu_{max}}\right)^{-4/3}\max\left(\frac{t_{\pm,\rm syn}}{t_{\rm dyn}},\ 1\right) \qquad \text{(E4)}$$

$$\simeq 4.8 M_9^{1/2} \dot{m}_{-4}^{-3/2} f_l^{-1} \Phi_{\rm rec,1.2}^{-3} \beta_{\rm rec,-1}^3 \ {\rm s},$$

$$t_{\pm,\rm syn} \simeq 3.3 \times 10^2 M_9 \dot{m}_{-4}^{-1} \Phi_{\rm rec,1.2}^{-2} \beta_{\rm rec,-1}^{-1} \ {\rm s}, \qquad \text{(E5)}$$

$$t_{\rm dyn} \simeq 9.8 \times 10^3 M_9 \ {\rm s}. \qquad \text{(E6)}$$

Since $t_{\rm ssa} < t_{\pm,\rm syn}$ for the entire energy range, the e^+e^- plasma should be thermalized without energy loss. M87 satisfies this condition.

For the cases with $t_{\rm dyn} < t_{\pm,\rm syn}$, which is satisfied in Sgr A*, the lepton plasma does not efficiently lose energy by radiation. Then, half of the injected plasma could move outward, and we can estimate the radio luminosity by

$$\mathcal{E}_{\rm blb} = \frac{1}{2}\dot{N}_{\gamma\gamma} T_{\rm dur} E_{\pm,\max}. \qquad \text{(E7)}$$

The other half of the injected plasma will fall to the SMBH. We consider that the SSA heating is ineffective in this case, regardless of the value of $t_{\rm ssa}$.

For the cases with $t_{\rm ssa} > t_{\pm,\rm syn}$ and $t_{\rm dyn} > t_{\pm,\rm syn}$, the lepton plasma loses energy by radiation. In this case, we use

$$\mathcal{E}_{\rm blb} = \frac{1}{4}\dot{N}_{\gamma\gamma} T_{\rm dur} E_{\pm,\max}, \qquad \text{(E8)}$$

where we assume that only the momentum parallel to the magnetic field is left after synchrotron cooling. Here, we consider that half of the injected plasma moves outward.

ORCID iDs

Shigeo S. Kimura ⓘ https://orcid.org/0000-0003-2579-7266
Kenji Toma ⓘ https://orcid.org/0000-0002-7114-6010
Hirofumi Noda ⓘ https://orcid.org/0000-0001-6020-517X
Kazuhiro Hada ⓘ https://orcid.org/0000-0001-6906-772X

References

Abramowski, A., Acero, F., Aharonian, F., et al. 2012, ApJ, 746, 151
Asano, K., & Mészáros, P. 2011, ApJ, 739, 103
Ball, D., Özel, F., Psaltis, D., Chan, C.-K., & Sironi, L. 2018, ApJ, 853, 184
Barrière, N. M., Tomsick, J. A., Baganoff, F. K., et al. 2014, ApJ, 786, 46
Barthelmy, S. D., Barbier, L. M., Cummings, J. R., et al. 2005, SSRv, 120, 143
Begelman, M. C., Blandford, R. D., & Rees, M. J. 1984, RvMP, 56, 255
Beskin, V. S. 2010, MHD Flows in Compact Astrophysical Objects (Berlin: Springer)
Blandford, R., Meier, D., & Readhead, A. 2019, ARA&A, 57, 467
Blandford, R. D., & Znajek, R. L. 1977, MNRAS, 179, 433
Brinkerink, C. D., Müller, C., Falcke, H. D., et al. 2019, A&A, 621, A119
Broderick, A. E., & Tchekhovskoy, A. 2015, ApJ, 809, 97
Camilloni, F., Dias, O. J. C., Grignani, G., et al. 2022, JCAP, 2022, 032
Cao, X. 2011, ApJ, 737, 94
Cemeljic, M., Yang, H., Yuan, F., & Shang, H. 2022, ApJ, 933, 55
Cerutti, B., Werner, G. R., Uzdensky, D. A., & Begelman, M. C. 2013, ApJ, 770, 147
Chen, A. Y., Yuan, Y., & Yang, H. 2018, ApJL, 863, L31
Cho, I., Zhao, G.-Y., Kawashima, T., et al. 2022, ApJ, 926, 108
Cohen, M. H., Cannon, W., Purcell, G. H., et al. 1971, ApJ, 170, 207
Comisso, L., & Sironi, L. 2018, PhRvL, 121, 255101
Comisso, L., & Sironi, L. 2019, ApJ, 886, 122
Cruz-Osorio, A., Fromm, C. M., Mizuno, Y., et al. 2022, NatAs, 6, 103
Degenaar, N., Miller, J. M., Kennea, J., et al. 2013, ApJ, 769, 155
Dexter, J., Tchekhovskoy, A., Jiménez-Rosales, A., et al. 2020, MNRAS, 497, 4999
EHT MWL Science Working Group, Algaba, J. C., Anczarski, J., et al. 2021, ApJL, 911, L11
Event Horizon Telescope Collaboration, Akiyama, K., Alberdi, A., et al. 2019a, ApJL, 875, L5
Event Horizon Telescope Collaboration, Akiyama, K., Alberdi, A., et al. 2019b, ApJL, 875, L6
Event Horizon Telescope Collaboration, Akiyama, K., Alberdi, A., et al. 2019c, ApJL, 875, L1
Event Horizon Telescope Collaboration, Akiyama, K., Algaba, J. C., et al. 2021a, ApJL, 910, L12
Event Horizon Telescope Collaboration, Akiyama, K., Algaba, J. C., et al. 2021b, ApJL, 910, L13
Event Horizon Telescope Collaboration, Akiyama, K., Alberdi, A., et al. 2022a, ApJL, 930, L12
Event Horizon Telescope Collaboration, Akiyama, K., Alberdi, A., et al. 2022b, ApJL, 930, L16
Ghisellini, G., & Svensson, R. 1991, MNRAS, 252, 313
Goldreich, P., & Julian, W. H. 1969, ApJ, 157, 869
Gravity Collaboration, Abuter, R., Amorim, A., et al. 2018, A&A, 618, L10
Guo, F., Li, H., Daughton, W., & Liu, Y.-H. 2014, PhRvL, 113, 155005
Guo, F., Li, X., Daughton, W., et al. 2021, ApJ, 919, 111
Guo, F., Liu, Y.-H., Li, X., et al. 2020, PhPl, 27, 080501
Hada, K. 2019, Galax, 8, 1
Hada, K., Kino, M., Doi, A., et al. 2013, ApJ, 775, 70
Hakobyan, H., Philippov, A., & Spitkovsky, A. 2019, ApJ, 877, 53
Kawashima, T., Ishiguro, S., Moritaka, T., Horiuchi, R., & Tomisaka, K. 2022, ApJ, 928, 62
Kawashima, T., Toma, K., Kino, M., et al. 2021, ApJ, 909, 168
Kim, J. Y., Krichbaum, T. P., Lu, R. S., et al. 2018, A&A, 616, A188
Kimura, M., Harada, T., Naruko, A., & Toma, K. 2021a, PTEP, 2021, 093E03
Kimura, S. S. 2022, arXiv:2202.06480
Kimura, S. S., Murase, K., & Mészáros, P. 2020, ApJ, 904, 188
Kimura, S. S., Murase, K., & Toma, K. 2015, ApJ, 806, 159
Kimura, S. S., Sudoh, T., Kashiyama, K., & Kawanaka, N. 2021b, ApJ, 915, 31
Kimura, S. S., & Toma, K. 2020, ApJ, 905, 178
Kimura, S. S., Toma, K., & Takahara, F. 2014, ApJ, 791, 100
Kino, M., Takahara, F., Hada, K., et al. 2015, ApJ, 803, 30
Kisaka, S., Levinson, A., & Toma, K. 2020, ApJ, 902, 80
Kisaka, S., Levinson, A., Toma, K., & Niv, I. 2022, ApJ, 924, 28
Komissarov, S. S. 2004, MNRAS, 350, 427
Komissarov, S. S. 2012, MNRAS, 422, 326
Komissarov, S. S., Vlahakis, N., Königl, A., & Barkov, M. V. 2009, MNRAS, 394, 1182
Kumar, P., & Zhang, B. 2015, PhR, 561, 1
Kuze, R., Kimura, S. S., & Toma, K. 2022, ApJ, 935, 159
Levinson, A., & Cerutti, B. 2018, A&A, 616, A184
Levinson, A., & Rieger, F. 2011, ApJ, 730, 123
Matsumoto, T., Chan, C.-H., & Piran, T. 2020, MNRAS, 497, 2385
Matsuoka, M., Kawasaki, K., Ueno, S., et al. 2009, PASJ, 61, 999
McEnery, J., van der Horst, A., Dominguez, A., et al. 2019, BAAS, 51, 245
McKinney, J. C., & Gammie, C. F. 2004, ApJ, 611, 977
McKinney, J. C., Tchekhovskoy, A., & Blandford, R. D. 2012, MNRAS, 423, 3083
Mizuno, Y. 2022, Univ, 8, 85

Mościbrodzka, M., Gammie, C. F., Dolence, J. C., & Shiokawa, H. 2011, ApJ, 735, 9

Murchikova, L., White, C. J., & Ressler, S. M. 2022, ApJL, 932, L21

Nakamura, M., Asada, K., Hada, K., et al. 2018, ApJ, 868, 146

Nakazawa, K., Mori, K., Tsuru, T. G., et al. 2018, Proc. SPIE, 10699, 106992D

Narayan, R., Sądowski, A., Penna, R. F., & Kulkarni, A. K. 2012, MNRAS, 426, 3241

Nathanail, A., & Contopoulos, I. 2014, ApJ, 788, 186

Neilsen, J., Nowak, M. A., Gammie, C., et al. 2013, ApJ, 774, 42

Nowak, M. A., Neilsen, J., Markoff, S. B., et al. 2012, ApJ, 759, 95

Ogihara, T., Ogawa, T., & Toma, K. 2021, ApJ, 911, 34

Parfrey, K., Philippov, A., & Cerutti, B. 2019, PhRvL, 122, 035101

Park, J., Hada, K., Kino, M., et al. 2019, ApJ, 887, 147

Porth, O., Mizuno, Y., Younsi, Z., & Fromm, C. M. 2021, MNRAS, 502, 2023

Ressler, S. M., White, C. J., Quataert, E., & Stone, J. M. 2020, ApJL, 896, L6

Ripperda, B., Liska, M., Chatterjee, K., et al. 2022, ApJL, 924, L32

Sari, R., Piran, T., & Narayan, R. 1998, ApJL, 497, L17

Sądowski, A., Narayan, R., Penna, R., & Zhu, Y. 2013, MNRAS, 436, 3856

Scepi, N., Dexter, J., & Begelman, M. C. 2022, MNRAS, 511, 3536

Sironi, L. 2022, PhRvL, 128, 145102

Sironi, L., Rowan, M. E., & Narayan, R. 2021, ApJL, 907, L44

Sironi, L., & Spitkovsky, A. 2014, ApJL, 783, L21

Sridhar, N., Sironi, L., & Beloborodov, A. M. 2021, MNRAS, 507, 5625

Sridhar, N., Sironi, L., & Beloborodov, A. M. 2022, arXiv:2203.02856

Takahashi, H. R., Ohsuga, K., Kawashima, T., & Sekiguchi, Y. 2016, ApJ, 826, 23

Takahashi, K., Toma, K., Kino, M., Nakamura, M., & Hada, K. 2018, ApJ, 868, 82

Tanaka, S. J., & Toma, K. 2020, MNRAS, 494, 338

Tchekhovskoy, A., Narayan, R., & McKinney, J. C. 2010, ApJ, 711, 50

Tchekhovskoy, A., Narayan, R., & McKinney, J. C. 2011, MNRAS, 418, L79

Toma, K., & Takahara, F. 2012, ApJ, 754, 148

Toma, K., & Takahara, F. 2013, PTEP, 2013, 083E02

Toma, K., & Takahara, F. 2016, PTEP, 2016, 063E01

Vlahakis, N., & Königl, A. 2003, ApJ, 596, 1080

Walker, R. C., Hardee, P. E., Davies, F. B., Ly, C., & Junor, W. 2018, ApJ, 855, 128

White, C. J., Stone, J. M., & Quataert, E. 2019, ApJ, 874, 168

Whitney, A. R., Shapiro, I. I., Rogers, A. E. E., et al. 1971, Sci, 173, 225

Wong, G. N., Ryan, B. R., & Gammie, C. F. 2021, ApJ, 907, 73

Yonetoku, D., Mihara, T., Doi, A., et al. 2020, Proc. SPIE, 11444, 114442Z

Yuan, F., & Narayan, R. 2014, ARA&A, 52, 529

Yuan, W., Zhang, C., Feng, H., et al. 2015, arXiv:1506.07735

Zamaninasab, M., Clausen-Brown, E., Savolainen, T., & Tchekhovskoy, A. 2014, Natur, 510, 126

Zenitani, S., & Hoshino, M. 2001, ApJL, 562, L63

Zenitani, S., & Hoshino, M. 2007, ApJ, 670, 702

Zhang, H., Sironi, L., & Giannios, D. 2021, ApJ, 922, 261